THE ASTROPHYSICAL JOURNAL, 466:1054–1066, 1996 August 1

NUMERICAL SIMULATION OF MAGNETIC RECONNECTION IN ERUPTIVE FLARES

TETSUYA MAGARA,[1,2] SHIN MINESHIGE,[1] TAKAAKI YOKOYAMA,[3] AND KAZUNARI SHIBATA[3]

Received 1995 September 15; accepted 1996 February 14

ABSTRACT

Prompted by the Yohkoh observations of solar flares, which have established the essential role of magnetic reconnection in the release of energy, we have studied the evolution of eruptive flares in some detail based on the reconnection model by means of the two-dimensional magnetohydrodynamic (MHD) simulations. We are interested in what factor affects the time evolution of solar flares and how the related phenomena, particularly observed loop-top source and plasmoid eruption, can be explained by this model. We have studied the dependence of the structure and evolution of the system on plasma β (ratio of gas pressure to magnetic pressure), adiabatic index, γ, and ρ_c (initial density in the current sheet). If the timescale and velocity are normalized by Alfvén time and Alfvén speed, respectively, we find that the main results (e.g., reconnection rate, plasmoid velocity, etc.) are rather insensitive to the plasma β. The ρ_c value, on the other hand, crucially affects the motion of a plasmoid: the ejection velocity of plasmoid grows in proportion to $\rho_c^{-1/2}$ in the early phase, which suggests that the observed plasmoid velocity can be reproduced when we assign $\rho_c \simeq 40\ \rho_0$ (initial density outside the current sheet). When adiabatic index γ is small, corresponding to the case of efficient thermal conduction, plasma heating will be generally suppressed, but the compression effect can be rather enhanced, which plays an important role in forming the high-density loop-top source. We discuss loop-top sources, plasmoid eruption, and the rise motion of a loop in comparison with the observations. Our simulations can well account for the existence of the loop-top, hard X-ray sources discovered in the impulsive flares. We concluded that both the impulsive flares and the LDE (long duration event) flares can be generally understood by the reconnection model for the *cusp-type* flares.

Subject headings: MHD — Sun: corona — Sun: flares — Sun: magnetic fields — Sun: X-rays, gamma rays

1. INTRODUCTION

Since the launch on 1991 August 30, the solar X-ray satellite *Yohkoh* has been collecting a variety of beautiful X-ray images of the Sun, which has promoted a great deal the research toward physical understandings of solar corona. Solar flares are one of the main targets of *Yohkoh*. So far, in fact, many details of time-dependent, spatially well-resolved flare structure have been revealed. Through extensive *Yohkoh* observations, it has been established that magnetic reconnection plays an essential role in the release of energy in flares (e.g., Tsuneta & Lemen 1993). In addition, *Yohkoh* has discovered many kinds of related phenomena, such as X-ray jets and X-ray plasma ejections (for a review, see Shibata 1995).

There are several different ways to classify solar flares (see Table 1). Here we distinguish between the LDE (long duration event) flare and the impulsive flare. Morphologically, the former has a cusp-shaped loop structure, while the latter does not, having only a simple loop structure. Since these two types of flares are different in appearance, it has been long thought that two distinct mechanisms may be operating for each. For example, the LDE flare (hereafter referred to as *cusp-type*) has been understood by the classical model for two ribbon flares; namely, it was long suspected that magnetic reconnection occurs above the loop top and most energy is released outside the loop (see Carmichael 1964; Sturrock 1966; Hirayama 1974; Kopp & Pneuman 1976). *Yohkoh* actually confirmed this hypothesis by the discovery of cusp-shaped loop structure in LDE flares (see Tsuneta et al. 1992). Impulsive flares (hereafter referred to as *non-cusp-type*), on the other hand, have been explained by the loop flare model, in which the main energy release occurs inside the loop, and magnetic reconnection does not take place outside the loop (Alfvén & Carlqvist 1967; Spicer 1977; Uchida & Shibata 1988). To sum up, it has been thought that a clear distinction exists between cusp-type and non–cusp-type flares.

Doubt has been cast on this interpretation, however, by the discovery of intense hard X-ray emission from above the bright soft X-ray loops in some observed impulsive limb flares (Masuda et al. 1994). Previously, this type of flares was classified as the non–cusp type, because only a closed loop was seen in soft X-rays. The presence of a hard X-ray source above the loop top has now established that an impulsive energy release occurs not inside, but outside the loop in at least some of non–cusp-type flares. Moreover, in the same impulsive limb flares (Masuda 1994), Shibata et al. (1995) found an X-ray signature of plasmoid, or filament eruptions, moving upward at about 50–400 km s^{-1}, which is of order of 10% of Alfvén velocity, V_A, because $V_A \propto 3000(B/100\ \mathrm{G})(n/10^{10}\ \mathrm{cm}^{-3})^{-1/2}$ km s^{-1} in the active region corona. Since plasmoid eruptions are one of the key features associated with the cusp-type flares, this also supports the idea that at least a part of the non–cusp-type flares may have a close similarity with the cusp-type flares (see also Shibata 1995). Now a question arises as to a relationship between the non-cusp-type and the cusp-type flare. To answer this question, we apply a fast magnetic reconnection mechanism based on Ugai (1986) to solar flare phenomena and study their evolution and structure, particularly plasmoid ejection and loop-top source, in detail. In the present

[1] Department of Astronomy, Faculty of Science, Kyoto University, Sakyo-ku, Kyoto 606-01, Japan.
[2] magara@kusastro.kyoto-u.ac.jp.
[3] National Astronomical Observatory, Mitaka, Tokyo 181, Japan.

TABLE 1

"TWO TYPES" OF FLARES

Observing Methods	Flare Type
Hα	Eruptive flares
	Confined flares
Yohkoh SXR	Cusp-type
	Non–cusp-type
HXR Light Curve	LDE (long duration event) flares
	Impulsive flares
Hα + *Skylab* SXR	Two-ribbon flares
	Simple loop flares
SXR	Arcade flares
	Loop flares
White-Light Coronagraph + Hα	CME-related flares
	Compact flares

NOTE.—The definition of these "two types" is not necessarily exact, and there are many flares showing intermediate natures. For example, some two-ribbon flares show impulsive nature, and vice versa. The point of this table is to show that solar observers have long thought that flares can be classified into two distinct types, although the criteria of classification depends very much on the observing methods.

study, we performed two-dimensional magnetohydrodynamic (MHD) simulations of solar magnetic reconnections, and we use the results from these simulations to investigate key characteristics of the cusp-type flares with possible applications to the non-cusp type as well. We consider a vertical current sheet, the bottom of which is fixed in a high-density region, such as chromosphere and photosphere. We give physical assumptions, basic equations, and methods of calculations in § 2. When a finite resistivity is given to a limited range over the transition layer as an initial perturbation, the fields start to dissipate. Then there arises an inflow toward the dissipated region, current density increases locally, and this increase eventually turns on "anomalous resistivity," which will be described in § 2.6, thus giving rise to a fast magnetic reconnection (see Ugai 1986). The numerical results will be presented in § 3. We then compare the calculations with the *Yohkoh* observations of solar flares in § 4. Since the observed ejection velocity of the plasmoid is quite small compared with some previous numerical results, we consider the factors causing this effect. In § 5, we discuss how flare structures can be explained on the basis of our results. The final section is devoted to conclusions.

2. MATHEMATICAL FORMULA AND PHYSICAL CONDITIONS

2.1. *Basic Equations*

We consider magnetized gas layers composed of an ideal gas. The effects of gravity are neglected for simplicity. Using the Cartesian coordinates, the basic equations are

$$\frac{\partial \rho}{\partial t} + \nabla \cdot (\rho \boldsymbol{v}) = 0 , \tag{1}$$

$$\rho\left[\frac{\partial \boldsymbol{v}}{\partial t} + (\boldsymbol{v} \cdot \nabla)\boldsymbol{v}\right] = -\nabla P + \frac{1}{4\pi}(\nabla \times \boldsymbol{B}) \times \boldsymbol{B} , \tag{2}$$

$$\frac{\rho^{\gamma}}{\gamma - 1}\left[\frac{\partial}{\partial t}\left(\frac{P}{\rho^{\gamma}}\right) + (\boldsymbol{v} \cdot \nabla)\left(\frac{P}{\rho^{\gamma}}\right)\right] = \frac{\eta}{4\pi}|\nabla \times \boldsymbol{B}|^2 , \tag{3}$$

$$\frac{\partial \boldsymbol{B}}{\partial t} = \nabla \times (\boldsymbol{v} \times \boldsymbol{B}) - \nabla \times (\eta \nabla \times \boldsymbol{B}) , \tag{4}$$

$$P = \frac{\rho \mathcal{R} T}{\mu} . \tag{5}$$

In addition, we use $\nabla \cdot \boldsymbol{B} = 0$ as an initial condition for equation (4). Here all the symbols, such as P, ρ, T, $\boldsymbol{v}$, and $\boldsymbol{B}$, have their usual meanings, γ is the adiabatic index, $\mathcal{R}$ is the gas constant, μ is mean molecular weight, and η is magnetic diffusivity.

2.2. *Units*

All the physical quantities in equations (1)–(5) have dimensions. Next we define the dimensionless variables by introducing three characteristic quantities: the reference length, L_0, the initial sound speed, $C_{s0}[\equiv(\gamma \mathcal{R} T_0/\mu)^{1/2}]$, where T_0 means the initial temperature, and density, ρ_0, outside the current sheet, respectively. The dimensionless variables (primed variables) are then

$$L' = \frac{L}{L_0} , \quad v' = \frac{v}{C_{s0}} , \quad \rho' = \frac{\rho}{\rho_0} , \quad P' = \frac{P}{\rho_0 C_{s0}^2} ,$$

$$T' = \frac{T}{C_{s0}^2/\gamma \mathcal{R}/\mu} , \quad B' = \frac{B}{\sqrt{\rho_0 C_{s0}^2}} , \quad t' = \frac{t}{L_0/C_{s0}} , \tag{6}$$

where L, v, ρ, P, T, B, t are the dimensional length, velocity, density, gas pressure, temperature, magnetic field, and time, respectively; η, the magnetic diffusivity, is also made dimensionless,

$$\eta' = \frac{\eta}{C_{s0} L_0} = R_m^{-1} , \tag{7}$$

where R_m is the magnetic Reynolds number.

2.3. *Initial Conditions*

Initially, we assume that total pressure, $P + (B^2/8\pi)$, is uniform in space. There is no gas motion, and magnetic fields have only the z-component. The initial conditions in dimensionless forms (after omitting primes for each quantity) are then

$$P(x, z) = \frac{1}{\gamma\beta}\frac{1}{\cosh^2[(3/2)\pi x]} + \frac{1}{\gamma} , \tag{8}$$

$$\frac{B_0^2}{8\pi} = \frac{1}{\gamma\beta} , \tag{9}$$

$$\boldsymbol{v} = 0 , \tag{10}$$

$$\boldsymbol{B}(x, z) = -B_0 \tanh\left(\frac{3}{2}\pi x\right)\hat{z} , \tag{11}$$

where B_0 is an initial magnetic field outside the current sheet and β is a parameter representing a ratio of gas pressure to magnetic pressure outside the current sheet. We study several models with different β and γ values, different initial density distribution, and different numerical resolutions, as listed in Table 2. For studying β-dependence, we assign $\beta = 0.2$ (model S; standard model), 0.5 (model B1), 1.0 (model B2), and 2.0 (model B3). Thermal conduction is not included. Instead, we calculate the low-γ case with $\gamma = 1.1$ (model G) as a limiting case of efficient thermal conduction, besides the normal-γ case with $\gamma = 5/3$ (model S).

For modeling the dense chromosphere and photosphere, we put a dense region between $z = 0$ and $z = 0.1$, in which

TABLE 2A

CALCULATED MODEL PARAMETERS

PARAMETER	MODEL									
	S	B1	B2	B3	D1	D2	D3	G	H1	H2
Resolution[a]	Low	Low	Low	Low	Low	Low	Low	Low	High	High
β	0.2	0.5	1.0	2.0	0.2	0.2	0.2	0.2	0.2	0.2
γ	5/3	5/3	5/3	5/3	5/3	5/3	5/3	11	5/3	11
v_c[b]	12	12	12	12	80	7	5	12	12	12
ρ_c[c]	6	6	6	6	1	11	16	6	6	6

TABLE 2B

FIGURE REFERENCES FOR MODELS

Model	Figure
S	3–5, 7–9, 13–14
B1	3–4, 8
B2	3–4, 8
B3	3–4, 8
D1	1, 5, 7
D2	5, 7
D3	5, 7
G	13, 14
H1	2, 6, 10, 12
H2	11, 12

[a] As for resolution, low means 100 × 100 grid cells (normal case), and high means 137 × 400 grid cells (fine-mesh case) in the present numerical simulation.

[b] v_c is the threshold value of anomalous resistivity (see eq. [19]).

[c] ρ_c is the initial density in the current sheet. For $\rho_c = 1$, initial density distribution is uniform and for $\rho_c = 6$, initial temperature distribution is uniform except in the enhanced density region.

density is taken to be about 10 times larger than in the other region in all models. In order to see how initial density distributions affect later evolution of the system, we calculated models with four different initial density profiles in the x-direction; a model with horizontally uniform density (model D1),

$$\rho(x, z) = -4.5 \tanh [50(z - 0.1)] + 5.5 , \quad (12)$$

and models with a density concentration at the current sheet,

$$\rho(x, z) = \frac{(\rho_c - 1) \cosh^{-2} [(3/2)\pi x] + 1}{0.45 \tanh [100(z - 0.1)] + 0.55} , \quad (13)$$

where ρ_c represents the initial density in the current sheet and is $\rho_c = 6$, 11, and 16 for models S, D2, and D3, respectively. Temperatures are then

$$T(x, z) = \gamma \frac{P(x, z)}{\rho(x, z)} , \quad (14)$$

in all cases (see eqs. [8], [12], and [13]).

As to the number of mesh points and the mesh spacings, we distinguish between two cases, the normal case and the fine-mesh case. In the normal case, the number of mesh points is $(N_x \times N_z) = (100 \times 100)$, and we used the uniformly distributed mesh points, $\Delta x = 0.08$ and $\Delta z = 0.24$. In the fine-mesh calculations, on the other hand, the numbers of mesh points is $(N_x \times N_z) = (137 \times 400)$. Furthermore, the mesh points are distributed uniformly in the z-direction, $\Delta z = 0.05$, but nonuniformly in the x-direction to obtain a good spatial resolution in the current sheet. Accordingly, the mesh spacings in the x-direction increase from $\Delta x = 0.02$ in the current sheet to $\Delta x = 0.1$ outside the current sheet.

In summary, model S is the standard model. Models B1–B3 have higher β values than model S. Model D1 is a model with a uniform density (horizontally), while models S, D2, and D3 have higher $\rho_c (> 1)$. The adiabatic index is $\gamma = 5/3$ except in model G, in which we take a low $\gamma = 1.1$. We also performed fine-mesh calculations, models H1 and H2, which have the same physical parameters as models S and G, respectively.

2.4. *Boundary Conditions*

Figure 1 illustrates the configuration of the simulated domain. We impose a free boundary condition at the upper boundary (at $z = 24$),

$$\frac{\partial B_x}{\partial z} = \frac{\partial v_x}{\partial z} = \frac{\partial v_z}{\partial z} = \frac{\partial P}{\partial z} = \frac{\partial \rho}{\partial z} = 0 , \quad \nabla \cdot \boldsymbol{B} = 0 , \quad (15)$$

an antisymmetric boundary condition along the z-axis (at $x = 0$),

$$v_x = B_z = \frac{\partial v_z}{\partial x} = \frac{\partial B_x}{\partial x} = \frac{\partial P}{\partial x} = \frac{\partial \rho}{\partial x} = 0 , \quad (16)$$

and symmetric conditions for the right boundary at $x = 8$,

$$v_x = B_x = \frac{\partial v_z}{\partial x} = \frac{\partial B_z}{\partial x} = \frac{\partial P}{\partial x} = \frac{\partial \rho}{\partial x} = 0 , \quad (17)$$

and for the lower boundary at $z = 0$,

$$v_z = B_x = \frac{\partial v_x}{\partial z} = \frac{\partial B_z}{\partial z} = \frac{\partial P}{\partial z} = \frac{\partial \rho}{\partial z} = 0 , \quad (18)$$

respectively. As for line tying at the base of the numerical domain, the presence of a dense layer at the base guarantees that the field lines are effectively stationary at the base. (However, some small movement of the field line at the base can be seen in Fig. 2.) Basic equations (1)–(5), together with the initial and boundary conditions, equations (8)–(18), were solved numerically using the modified Lax-Wendroff method (see, e.g., Shibata et al. 1989).

In actual calculations, we solve only the equations over a half-domain ($x \geq 0$). When illustrating the results, we doubled the calculation domain, assuming a mirror symmetry at $x = 0$; namely, any physical quantities at $(x < 0, z)$ are set to be equal to those at $(-x, z)$ at the same time, t.

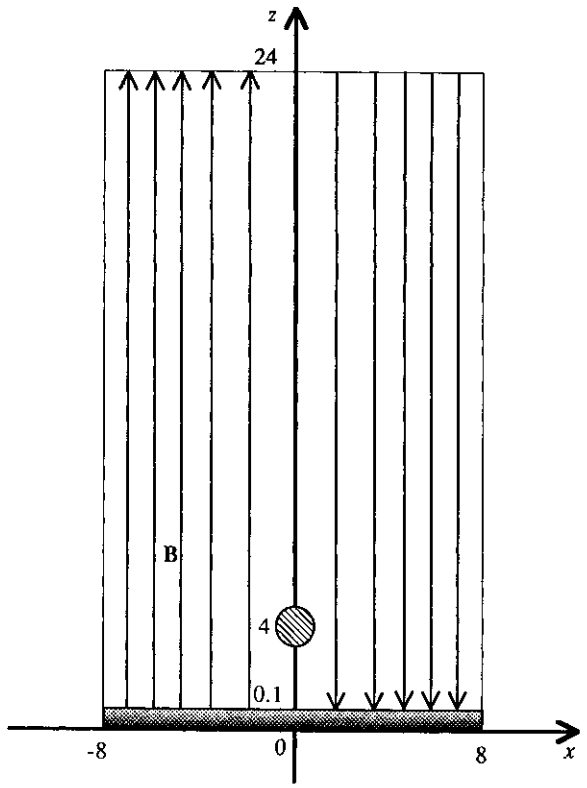

FIG. 1.—Initial configuration of the simulated domain in the (x, z)-plane. Magnetic field lines are set to be parallel to the z-axis with opposite directions on the right ($x > 0$) and left ($x < 0$) sides. The hatched and shaded areas represent the regions where the artificial resistivity is turned on for the initial perturbation ($0 < t < 0.6$) and the initial density is enhanced for modeling the lower dense atmosphere, respectively. In actual simulations, we solve the basic equations only over a half-domain (at $x > 0$), assuming a mirror symmetry with respect to the z-axis.

2.5. *Initial Perturbations*

Initially, the diffusivity coefficient is set to be $\eta = 0$ everywhere, except in a narrow region of $[x^2 + (z - 4.0)^2]^{1/2} \leq 0.8$ (a shaded area in Fig. 1), in which $\eta = 1/30$ is assigned for a finite time, $0 < t < 0.6$. Because of a finite value of resistivity in a narrow region, magnetic fields can dissipate initially, which raises the inflow toward the neutral point. Current densities will then increase in the neutral layer, eventually turning on anomalous resistivity (see below).

2.6. *Anomalous Resistivity*

We may assume safely that a "fast magnetic reconnection" is responsible for a violent energy release in flares. Among several physical processes capable of causing fast reconnections, anomalous resistivity will probably be one of the most important factors. Anomalous resistivity is known to have a close relationship with plasma microturbulence (see Parker 1979). Suppose that the strength of magnetic fields changes so rapidly in space that the electron drift velocity can exceed its thermal velocity, $u = (kT/m)^{1/2}$, where k is the Boltzmann constant, T is temperature, and m is an electron mass. Then the mean flow of electrons is expected to excite plasma microturbulence, which provides a seed for anomalous resistivity. It is important to note that anomalous resistivity can localize the diffusion region into a fairly small area, thereby yielding the "Petschek type" configuration, which is actually favored in terms of causing a fast magnetic reconnection (Yokoyama & Shibata 1994).

We assume the following form for the anomalous resistivity in the present study except that the η is over 300, when η is constantly set to 300:

$$\eta = \begin{cases} \eta_c\left(\left|\dfrac{v_d}{v_c}\right| - 1\right), & \text{for } |v_d| \equiv \left|\dfrac{j}{\rho}\right| > |v_c|, \\ 0, & \text{otherwise}, \end{cases} \tag{19}$$

were v_d is a relative ion-electron drift velocity, v_c is a threshold velocity, and η_c is a constant representing a magnitude of resistivity (see Ugai 1986). In the present study, we assign $v_c = 5, 7, 12, 80$ (see Table 1) and $\eta_c = 1/15$.

3. STRUCTURE AND EVOLUTION

3.1. *Evolution of System*

First we overview the evolution of the system. Figure 2 depicts how magnetic reconnection proceeds in model H1 ($\beta = 0.2$, $\gamma = 5/3$). Here the solid lines represent magnetic field lines, and the overlying arrows show the velocity. Elapsed times are $t = 0$, 6, 12, and 18 (L_0/C_{s0}) in the Figures 2*a*–2*d* respectively. Note that only a part of the calculated domain, $(-4, 0) \leq (x, z) \leq (4, 20)$, is displayed here.

A fast magnetic reconnection sets out at $t \sim 6$ (Fig. 2*a*) and a plasmoid begins to form. As magnetic reconnection still proceeds, the plasmoid moves upward, becoming larger in size. Reconnected flux flows downward, and a closed-loop structure appears at $z \sim 2$ (Fig. 2*c*). Finally, a cusp structure is formed at the top of the lower closed loop (at $z \sim 3$) after $t = 18$ (Fig. 2*d*). On the whole, these features are consistent with the previous results (e.g., Forbes & Priest 1982).

We have run similar models but with different β-values (models B1–B3; see Table 2). The β-dependence of the reconnection rate is depicted in Figure 3*a*. In this figure, we plot the time evolution of the reconnection rates for $\beta = 0.2$, 0.5, 1.0 and 2.0. The reconnection rate was derived from the electric field at the neutral point (see Forbes & Priest 1982). By using Ohm's law $\{\eta \boldsymbol{J} = (c^2/4\pi)[\boldsymbol{E} + (\boldsymbol{v}/c) \times \boldsymbol{B}]$ in cgs units$\}$, the electric field at the neutral point is proportional to $\eta \boldsymbol{J}$ because $\boldsymbol{v} \times \boldsymbol{B} = 0$ at this point. Evidently from Figure 3*a*, the lower β is, the more quickly the system evolves. Therefore, when β is sufficiently low ($\beta \ll 0.1$), as in the solar corona, we expect reconnection to proceed more violently.

Next, we illustrate in Figure 3*b* the normalized reconnection rate, $\eta j/V_{A0} B_0$ (where V_{A0} is the initial Alfvén velocity outside the current sheet), against the normalized time by the Alfvén transit time, $t_{A0} = 1/V_{A0}$. It is interesting to note that Figure 3*b* shows similar time variation for all models with different β (especially lower β models, S and B1) in contrast with Figure 3*a*. This implies that the evolution of the system is controlled by the magnetic field; in other words, the Alfvén transit time gives a fundamental timescale for this system. Figure 4 plots the time evolution of inflow velocity of plasmas toward the neutral point and also supports the above implication. In this figure, the elapsed time is normalized by t_{A0}, and the inflow velocity is normalized by V_{A0}. Again, four models show similar behavior. Since the inflow velocity is related to the reconnection rate,

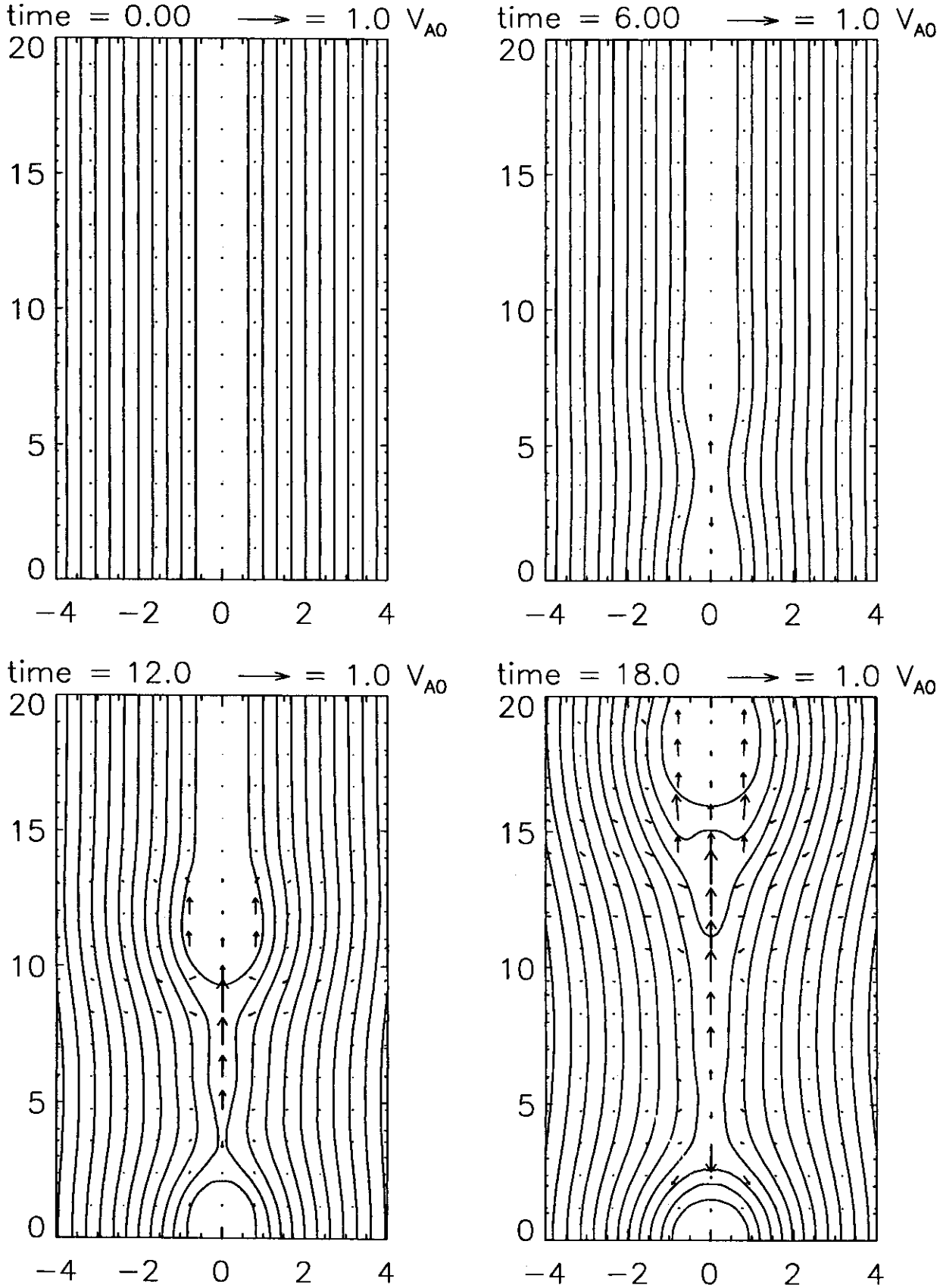

FIG. 2.—Development of magnetic reconnection in the standard model (model S). Magnetic field lines are illustrated by the solid lines, while the arrows indicate velocity fields normalized by V_{A0}, the Alfvén velocity outside the current sheet.

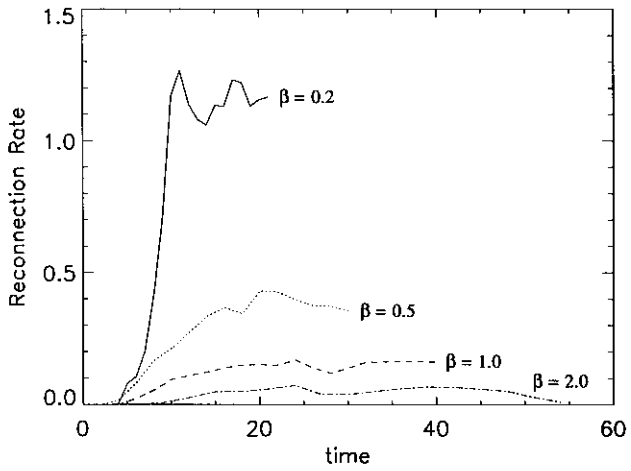

FIG. 3a

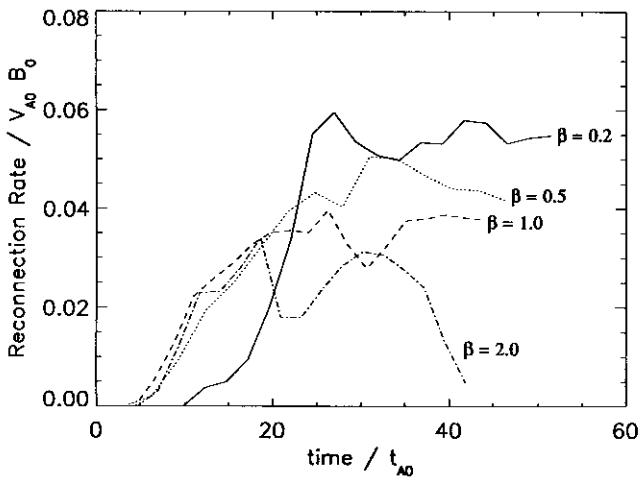

FIG. 3b

FIG. 3.—(*a*) Time variations of the reconnection rates for several values of β; $\beta = 0.2$, 0.5, 1.0, and 2.0, respectively (models S and B1–B3). Time is normalized by the sound crossing time outside the current sheet. (*b*) Same as (*a*) but for the time (*horizontal axis*) being normalized by the Alfvén transit time outside the current sheet t_{A0} and the reconnection rate (*vertical axis*) by $V_{A0} B_0$.

we expect that the dynamical evolution of the system is characterized by the Alfvén transit time.

We then study the dependence of the inflow velocity on ρ_c by comparing model S, D1, D2, and D3. Figure 5 plots time variation of the inflow velocity normalized by V_{A0} and t_{A0} for different ρ_c. This figure shows that the inflow velocity is unaffected by changing ρ_c; that is, the maximum values of $V_{\text{inflow}} \sim 0.1 V_{A0}$. The initial rapid increase phase is different from one case to the next because this phase is characterized not by t_{A0} but by $t_{Ac} = 1/V_{Ac}$, where V_{Ac} and t_{Ac} are the initial Alfvén velocity and Alfvén transit time inside the current sheet, respectively. Roughly, this phase corresponds to $6 \leq t/t_{A0} \leq 10$ for $\rho_c = 1.0$, $15 \leq t/t_{A0} \leq 25$ for $\rho_c = 6.0$, $20 \leq t/t_{A0} \leq 34$ for $\rho_c = 11.0$, and $24 \leq t/t_{A0} \leq 40$ for $\rho_c = 16.0$. From Figures 4 and 5, the inflow velocity is about 10% of V_{A0} in all cases, independently of the values of β and ρ_c.

3.2. *Structure and Motion of Plasmoid*

Let us turn to the time evolution of the plasmoid. The Figure 6*a* (Plate 25) displays temperature contours for model H1. It is found that high-temperature regions lie along the magnetic fields extending out from the neutral point. The highest temperature exists at the bottom of the plasmoid ($z \sim 14.5$). The accelerated plasma emerging from the neutral point collides with the bottom of the plasmoid (at $z \sim 14.5$) and forms a fast shock there. Plasma flow occurs from the neutral point upward along the magnetic field lines surrounding the plasmoid, thereby heating plasmas at its surface. (Since thermal conduction is not included in the present simulations, heat transfer takes place only by the bulk flow of hot gas. In reality, thermal conduction should play an important role in the heat transport.) In addition, slow shocks appear inside such hot regions, thus forming a triangular high-temperature area $(-1, 10) \leq (x, z) \leq (1, 14.5)$ with the fast shock.

Let us see, next, the density contours in Figure 6*b*. At first sight, this figure looks quite differently from Figure 6*a*. Density is maximum at the center of the plasmoid (at $z \sim 15$) and is about 10 times larger than the value outside the plasmoid. The dense matter confined in the plasmoid comes mostly from inside the current sheet. Therefore, if the plasma is initially more concentrated along the current sheet, the plasmoid will have higher density. This is of great importance when discussing the observational appearance

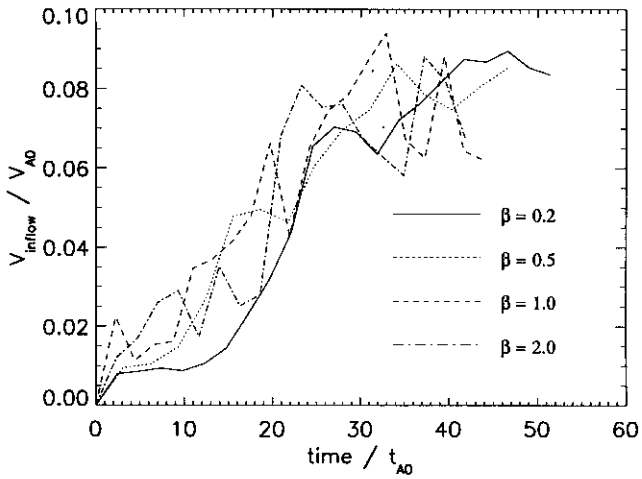

FIG. 4.—Time variations of the inflow velocity toward the neutral point for the same models as those in Fig. 3. The velocity and the time are normalized by V_{A0} and t_{A0}, respectively. The plotted inflow velocity is the average over an interval between $x = 0.8$ and 1.6.

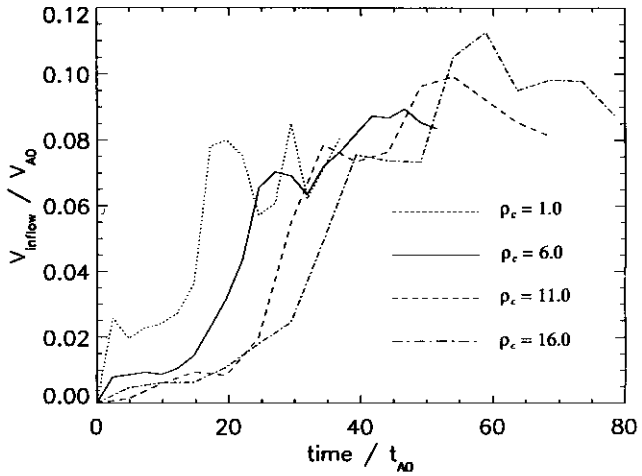

FIG. 5.—Same as Fig. 4, but for different values of ρ_c (models S and D1–D3).

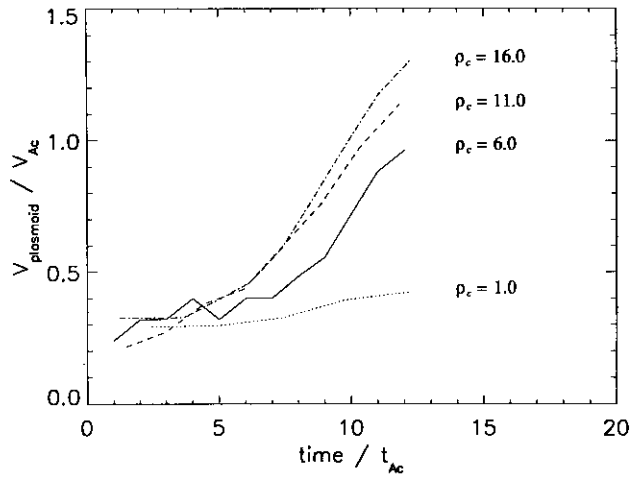

FIG. 7a

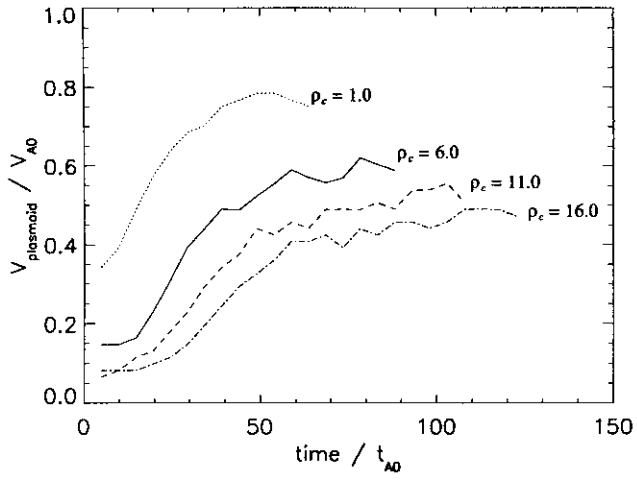

FIG. 7b

FIG. 7.—(*a*) Time variations of the velocity of the ejected plasmoid for different values of ρ_c (models S and D1–D3). The velocity and the time are normalized by the Alfvén velocity V_{Ac} and the Alfvén transit time t_{Ac} inside the current sheet, respectively. (*b*) Same as (*a*), but for the time being normalized by t_{A0} and the velocity by V_{A0}.

of the plasmoid. Since the emissivity is more sensitive to density than temperature, the bright plasmoid in soft X-ray seems to contain high-density plasma.

As for the motion of the plasmoid, the $\boldsymbol{J} \times \boldsymbol{B}$ force plays a main role in accelerating it. Large upward velocities are found in the regions surrounding the core of the plasmoid. This is because large acceleration occurs due to magnetic tension force by bent magnetic fields, so that the matter inside the plasmoid can be pushed strongly upward.

The effect of ρ_c on the plasmoid motion is displayed in Figures 7*a* and 7*b*. We measure the variation of the zero point (center of plasmoid) with time and calculate its velocity. In the early phase, it is well understood that the velocity of a plasmoid is proportional to that of the outflow from the neutral point; that is, $(1/2)\rho_c V_{outflow}^2 \sim B_0^2/8\pi$, so $V_{plasmoid} \propto V_{outflow} = V_{Ac} \equiv B_0/(4\pi\rho_c)^{1/2}$. Figure 7*a* shows the temporal variation of its velocity normalized by t_{Ac} and V_{Ac}. All models show similar profiles in this early phase (corresponding to $0 \leq t/t_{Ac} \leq 7$), when the reconnection rate increases rapidly. Therefore, we find $V_{plasmoid} \propto \rho_c^{-1/2}$ in this phase. In the late phase ($t/t_{Ac} \geq 7$), however, differences in $V_{plasmoid}$ grow among the different models. This is because as the plasmoid grows larger in size, the matter outside the current sheet drains into the plasmoid, which weakens the effect of ρ_c. Instead, the plasmoid motion is affected more by the outside density, ρ_0. Figure 7*b*, whose abscissa and ordinate are normalized by V_{A0} and t_{A0}, supports this consideration because all show similar variation after the early increase phases; that is, the plasmoid velocity eventually becomes almost constant with time, which is consistent with the results of Ugai (1995). (Differences among the terminal velocities are caused by different accelerations in the early phase.) From these results, we see that the dependence of the plasmoid velocity on the initial density changes from $\propto \rho_c^{-1/2}$ in the early phase to $\propto \rho_0^{-1/2}$ in the late phase.

Next we display the β-dependence of $V_{plasmoid}$ in Figure 8. These figures imply that $V_{plasmoid}$ normalized by V_{A0} has only a weak dependence on β, $V_{plasmoid}/V_{A0} \sim 0.54\beta^{0.06}$. (In Fig. 8, the velocity is defined by the mean velocity, which is described in § 3.3.) In conclusion, the plasmoid motion (normalized by V_{A0} and t_{A0}) depends sensitively on the initial density inside the current sheet, ρ_c, rather than the plasma β.

3.3. *Apparent Rise Motion of Reconnected Loop*

Next we turn our attention to the closed loop structure below the reconnection point. Figure 9 illustrates by the thick line how the top of the closed loop moves upward with time for model S with $\beta = 0.2$. To figure out the loop-top motion, we select first some representative magnetic field lines which were reconnected and move away from the neutral point. As time goes on, each field line moves downward, and we plot the temporal variation of its height on the z-axis (where $x = 0$) by the thin lines. (This downward movement appears to have been observed by *Yohkoh*; see Hiei & Hundhausen 1996.) Then we define the place of the loop top to be the first big-bend point, which is marked with a simple asterisk on each thin line. Finally we fit these points by a curve fitting and plot the results of the fitting by the thick line. Roughly, we find that the loop top moves in proportion to $t^{0.7}$; that is, the loop rises rapidly at first but is gradually decelerated later.

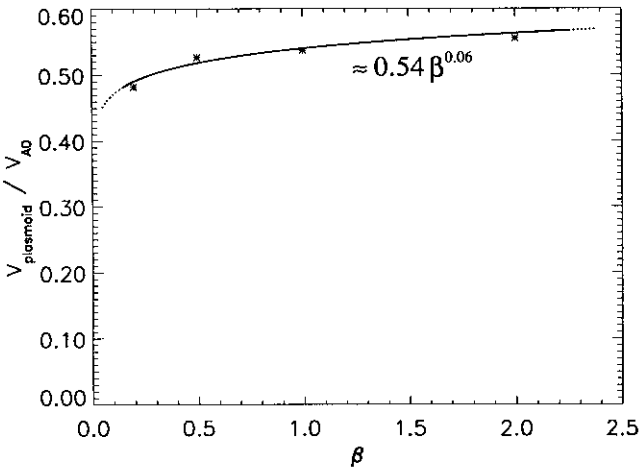

FIG. 8.—The β dependence of the inflow velocity. Roughly, $V_{plasmoid}/V_{A0} \propto \beta^{0.06}$.

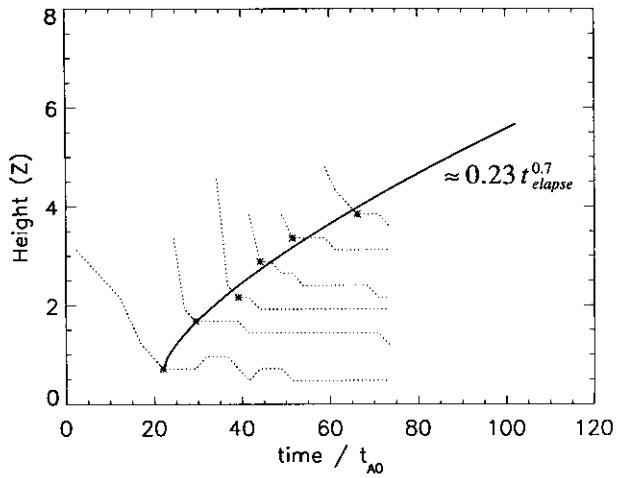

FIG. 9.—Upward motion of the loop top for the standard model (model S). Every thin dotted line represents the time variation of the height (z) of the representative field line at $x = 0$. Stars indicate the first turning points in each thin line, which we regard as the site of the loop top. The thick curve is a power-law fit to the heights of the turning points.

We made the same figures for cases with $\beta = 0.5$, 1.0, and 2.0 and derived the mean rise velocities of the loops for each case. The mean velocity is a velocity averaged over a time span after the early phase of a rapidly increasing reconnection rate ($t/t_{A0} \geq 30$). Table 3 lists the mean velocities of the inflow, upward motion of plasmoid, and rise motion of the loop. The relation between the rise velocity of the loop and inflow velocity will be discussed in § 4.

3.4. *Structure of Loop*

Next we examine the detailed loop structure. As was mentioned above, we calculated models G and H2 (low-γ models) to study the role of thermal conduction. In this sense, we may assume that the low-γ case roughly simulates the system in the phase at which thermal conduction works efficiently. (Precisely speaking, since the thermal conduction works well only along the field lines, the low-γ case cannot allow for the thermal conduction effect throughout the system. Therefore, it may be misleading to say that the low-γ case corresponds to this phase of evolution. However, the low-γ model can still simulate some parts of the system in the presence of high-temperature region and large heat flow.) With these considerations in mind, we study the loop-top structure of less efficient thermal conduction by model H1 and of efficient thermal conduction by model H2, respectively.

Figure 10*a* (Plate 26) is composed of the temperature contours (*top left*), the density contours (*top right*), the pressure contours (*bottom left*), and current density contours (*bottom right*) for model H1 at $t = 10$. Overlain are the magnetic field lines (*solid lines*) and the velocity fields (*arrows*). Figures 10*b* and 10*c* are the one-dimensional variations of representative physical quantities, such as fast-mode Mach number (M_a), temperature (T), current density (Jy), gas pressure (Pg), magnetic pressure (Pm), density (ρ), and the x-component of the magnetic field ($|B_x|$), near the loop top along the z-axis and horizontal line, respectively.

The maximum temperature is reached near the neutral point, where the temperature is about 8 times as hot as that of the surroundings. There is little matter present near the neutral point, since plasmas in this region have been pushed away due to high magnetic tension force around the neutral point. The loop top is also hot; it is about 6 times as hot as the ambient region. Between these hot regions, there formed a triangular hot area $(-0.5, 1.7) \leq (x, z) \leq (0.5, 3.5)$ by slow and fast shocks (see Fig. 10*a*). Figure 10*b* shows clearly the formation of a fast shock and the density increases behind this, and Figure 10*c* indicates that there exists a hot and dense region between slow shocks. This high-temperature and high-density region is produced by the fast and slow shock and confined at the loop top.

Figures 11*a*–11*c* are the same as Figures 10*a*–10*c* but for model H2. The elapsed time is $t = 19$. Figure 11*a* (Plate 27) shows that temperature is relatively high both at the neutral point and in the loop top, but temperature enhancements are only higher by a factor of 2. On the other hand, the density enhancement at the loop top is larger than model H1; it is about 3 times denser than the ambient region (see Fig. 11*c*). In the low-γ case, therefore, temperature cannot increase much, while density can. Matter can thus be compressed more when γ is smaller.

Since this simulation does not include the radiative cooling effect, there remain hot regions inside the loop. But in reality, the cooling effect can easily decrease the temperature inside the loop to form Hα postflare loops (see § 6).

There is one noteworthy feature present in both Figure 10*c* and Figure 11*c*; the high-density region is confined by "magnetic pressure walls." Thus, the dense region can stay at the loop top for a long time, since the magnetic walls prevent the gas from draining downward.

TABLE 3

β-DEPENDENCE OF VARIOUS VELOCITIES

PARAMETER	MODELS S ($\beta = 0.2$)	B1 ($\beta = 0.5$)	B2 ($\beta = 1.0$)	B3 ($\beta = 2.0$)
V_{inflow}[a]	0.19(0.079)	0.12(0.076)	0.078(0.0711)	0.057(0.073)
$V_{plasmoid}$[b]	1.2(0.48)	0.82(0.53)	0.59(0.54)	0.43(0.56)
V_{loop}[c]	0.18(0.075)	0.10(0.066)	0.071(0.065)	0.037(0.048)
V_{A0}[d]	2.5	1.5	1.1	0.77

NOTE.—The numbers in parentheses indicate the values normalized by V_{A0}.

[a] V_{inflow} is the inflow velocity toward the neutral point.
[b] $V_{plasmoid}$ is the ejection velocity of the plasmoid.
[c] V_{loop} is the rise velocity of the loop.
[d] V_{A0} is the initial Alfvén velocity outside the current sheet.

3.5. *Effect of γ*

Finally we describe the γ-dependence. Figure 12 compares the time evolution of reconnection rates for the normal-γ case ($\gamma = 5/3$) and the low-γ case ($\gamma = 1.1$). Time and reconnection rate are normalized by t_{A0} and $V_{A0} B_0$, respectively. It is interesting to note that the evolution of the low-γ case is more violent than the normal-γ case; that is, the system undergoes a rapid increase and subsequent decrease in the reconnection rate. Therefore, if the thermal conduction works more efficiently, flares exhibits more drastic evolution. Figure 13 displays the time evolution of the ratios of the thermal and kinetic energies to the released magnetic energy for the normal-γ case and for the low-γ case, respectively. The formulation is

$$\frac{\Delta E}{\Delta E_m} = \frac{|E(t) - E(0)|}{|E_m(t) - E_m(0)|}, \tag{20}$$

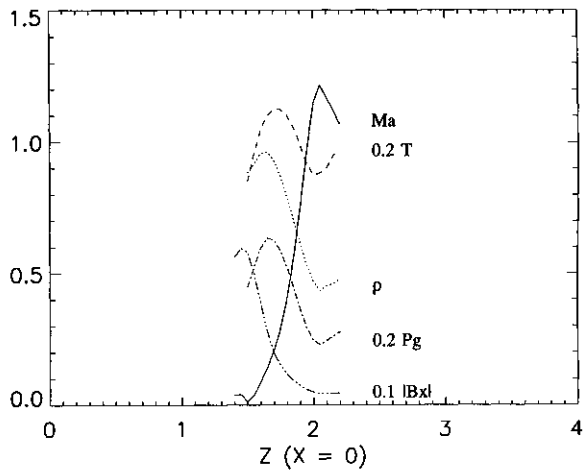

FIG. 10*b*

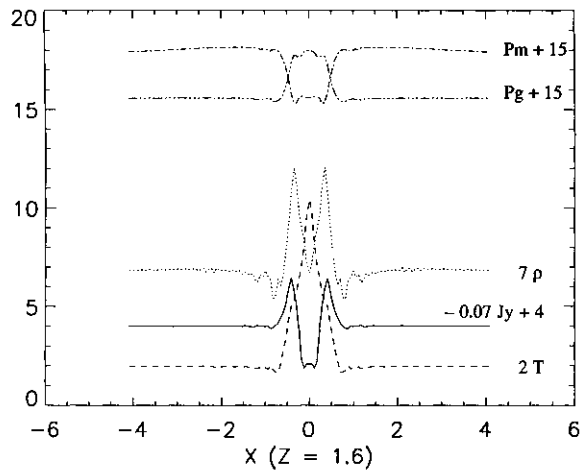

FIG. 10*c*

where $E(t)$ represents the kinetic or thermal energies integrated over a region of $(0, 0) \leq (x, z) \leq (8, 19.2)$, and E_m is the magnetic energy (t indicates time normalized by t_{A0}),

$$E(t) = \begin{cases} \int_0^{x_1} \int_0^{z_1} \frac{1}{2} \rho v^2 \, dx \, dz & \text{for kinetic energy} , \\ \int_0^{x_1} \int_0^{z_1} \frac{P}{\gamma - 1} \, dx \, dz & \text{for thermal energy} , \end{cases} \tag{21}$$

$$E_m(t) = \int_0^{x_1} \int_0^{z_1} \frac{B_0^2}{8\pi} \, dx \, dz , \tag{22}$$

where x_1 and z_1 are 8.0 and 19.2, respectively. We determine the time span during which there is little outflow from the boundary. The earliest phase ($0 \leq t/t_{A0} \leq 2$) corresponds to the time range in which the initial perturbation proceeds. It is noticeable that 80% of the released magnetic energy is initially converted to the thermal energy and 20% to the kinetic energy in the normal-γ case (denoted by the thick line). While the thermal energy tends to decrease with time, the kinetic energy increases gradually, reaching about 40% of the released magnetic energy at maximum. This implies that a large amount of the released energy is lost in the form of kinetic energy. In the low-γ case (*thin line*), in contrast, the released magnetic energy is converted more to kinetic energy. Thus, we expect that magnetic energy can be converted more to kinetic energy than thermal energy in the presence of efficient thermal conduction.

Next, we plot in Figures 14*a* (the normal-γ case) and 14*b* (the low-γ case) the decreasing rate of magnetic energy, the rate of work due to Lorentz force, the Joule heating rate, and the input magnetic flux crossing over the line at $x = 4$ with $0 \leq z \leq 19.2$, respectively. This time span is the same as Figure 13. Energies are integrated over the calculated region of $(0, 0) \leq (x, z) \leq (4, 19.2)$.

$$\left| \frac{\partial E_m}{\partial t} \right| = \left| \frac{\partial}{\partial t} \int_0^{x_2} \int_0^{z_2} \frac{B_0^2}{8\pi} \, dx \, dz \right| , \tag{23}$$

the rate of work due to Lorentz force

$$= \int_0^{x_2} \int_0^{z_2} (\boldsymbol{J} \times \boldsymbol{B}) \cdot \boldsymbol{v} \, dx \, dz , \tag{24}$$

$$\text{Joule heating rate} = \int_0^{x_2} \int_0^{z_2} \frac{\eta}{4\pi} j^2 \, dx \, dz , \tag{25}$$

$$\text{Input flux} = \left| \int_0^{z_2} \left(\frac{\boldsymbol{E} \times \boldsymbol{B}}{4\pi} \right)_{x = x_2} dz \right| , \tag{26}$$

where x_2 and z_2 are 4 and 19.2, respectively.

It is found that the $\boldsymbol{J} \times \boldsymbol{B}$ acceleration is dominant compared with the Joule heating, which is consistent with the

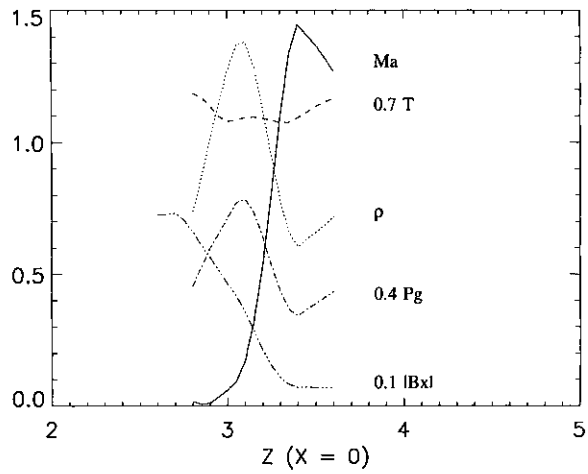

FIG. 11*b*

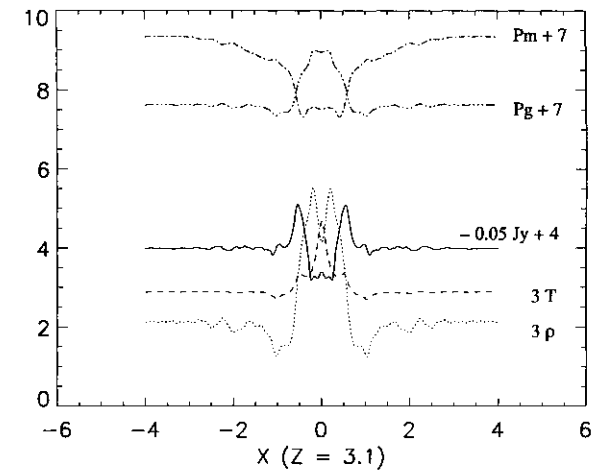

FIG. 11*c*

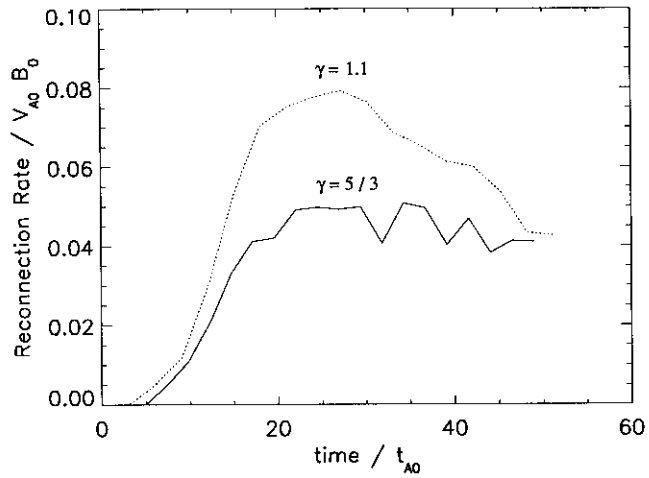

FIG. 12.—Time variations of the reconnection rates for $\gamma = 5/3$ and $\gamma = 1.1$ cases (models H1 and H2). Time is normalized by r_{A0}, and reconnection rate is normalized by $V_{A0} B_0$.

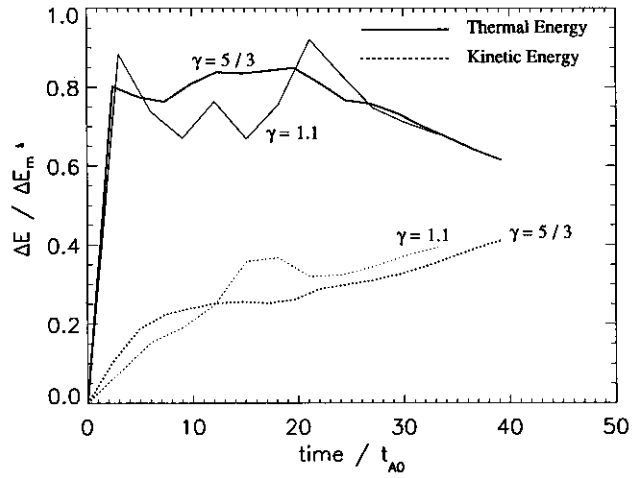

FIG. 13.—Time variations of the increases of both thermal (*solid lines*) and kinetic (*dashed lines*) energies as to the decrease of magnetic energy from their initial values for $\gamma = 5/3$ and 1.1 (models S and G). The energies are integrated over the calculated domain of $(0.0, 0.0) \leq (x, z) \leq (8.0, 19.2)$.

results of Sato & Hayashi (1979). Compared with the normal-γ case, the low-γ case shows the suppression of Joule heating but the enhancement of the rate of work due to the Lorentz force, which implies that the evolution of the low-γ case is more dynamical. The oscillation patterns are due to the reflections of magnetohydrodynamic waves at the side boundaries ($x = 8$).

4. COMPARISON WITH *Yohkoh* OBSERVATIONS

4.1. *Loop-Top Sources*

Masuda et al. (1994) found a hard X-ray impulsive source well above the soft X-ray flaring loop in the impulsive phase of flares. In the gradual phase, the more long-lived source continues to exist near the loop top. We try now to interpret these observational facts in relation to the present simulations.

Let us begin with the impulsive phase. It is very likely that a hard X-ray impulsive source may be formed near the loop top, where the reconnection jet emerging from the neutral point collides with the material inside the loop, thus forming a fast shock. From the simulation of the phase when the reconnection rate rapidly increases, in fact, we found that the loop-top has a high-temperature and high-density region (see Fig. 10) encompassed with the fast shock and slow shocks, which probably emit strong radiation.

It is plausible to assume that after being heated by the thermal conduction originating from near the neutral point, the chromospheric gas evaporates and rises along the loop, emitting soft X-rays. The soft X-ray flaring loop is thus formed. We suppose that the gradual phase corresponds to the phase in which slow and fast shocks are formed in the loop filled with evaporated plasmas. As for this phase, we compare the low-γ case with observation because in this phase the thermal conduction becomes effective. Figure 11 shows that the loop top becomes about 3 times denser than the ambient plasma, and the "magnetic pressure walls" form around this high-density core (see Fig. 11). These walls can confine the high-density core at the loop top for a long time, explaining the presence of a long-lived loop-top source during the gradual phase (see Acton et al. 1992; Feldman et al. 1994). [In the present simulation, this core continued to exist to the end, say, $t \simeq 60 t_{A0}$, which corre-

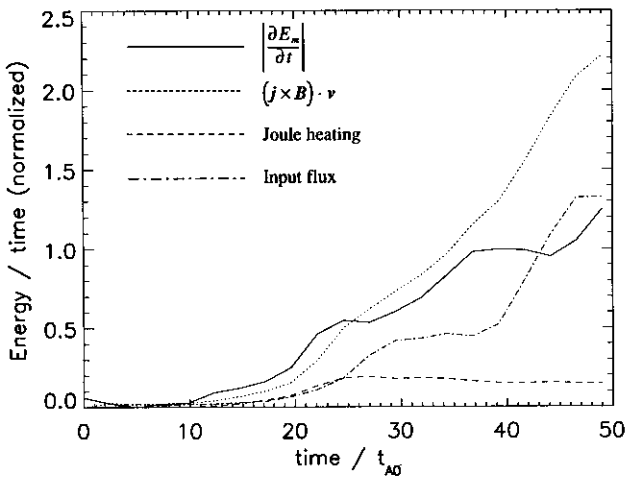

FIG. 14*a*

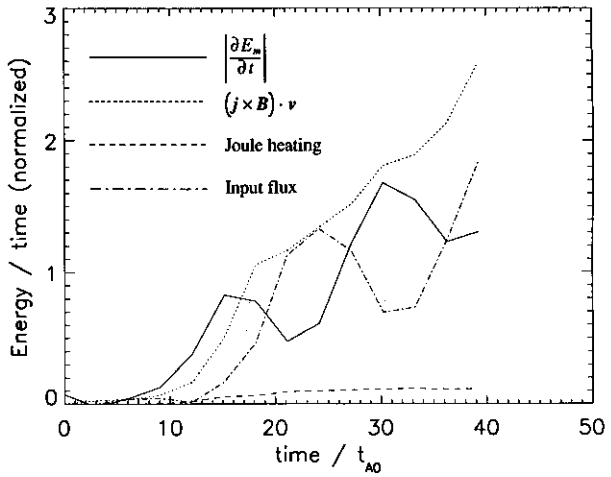

FIG. 14*b*

FIG. 14.—(*a*) Time variations of the energy generation rates for the standard model (model S). Solid, dotted, dashed, and dot-dashed lines represent, respectively, the decrement in magnetic energy, the work done by Lorentz force, Joule heating, and the energy flux input from the side boundary ($x = 4.0$ and $0 \leq z \leq 19.2$). (*b*) Same as (*a*), but for the low-γ model (model G).

sponds to several minutes if we assume $V_{A0} \sim 1000$ km s^{-1} and loop height $\sim 20{,}000$ km ($L_0 \sim 6000$ km).]

4.2. *Motion of Plasmoid*

Next we will discuss the motion of the plasmoid. The velocity of the plasmoid is observationally about 50–400 km s^{-1} in the early phase (see Shibata 1995). The Alfvén velocity in the active region corona is estimated to be

$$V_{A0} \simeq 3000(B/100\ \mathrm{G})(n_e/10^{10}\ \mathrm{cm}^{-3})^{-1/2}\ \mathrm{km\ s}^{-1}.$$

Hence, $V_{\mathrm{plasmoid}} \simeq 0.1 V_{A0}$. On the other hand, from our simulations, V_{plasmoid} is about $0.25 V_{A0}$ in the standard model ($\rho_c = 6\rho_0$). (This value is estimated in the early phase: $t_{A0} \sim 20$, see Fig. 7*b*.) The reasons for this discrepancy may be as follows: First, the initial density in the current sheet, ρ_c, may be much larger than the values we set. As mentioned above, we find that the velocity of the plasmoid can be reduced by an increase of ρ_c. Since in the early phase the ρ_c dependence of the ejection velocity follows $V_{\mathrm{plasmoid}}/V_{A0} \propto \rho_c^{-1/2}$, the required density in the current sheet is $\rho_c \sim 40\ \rho_0$. In contrast, Figure 4 indicates that the reconnection processes (characterized by V_{inflow}) can hardly be affected by changing ρ_c. To conclude, we need to assign large ρ_c values so that we can explain observed V_{plasmoid} and reconnection rates simultaneously.

4.3. *Inflow Velocity*

Finally, we give one prediction concerning the inflow velocity to the neutral point. Table 3 shows the relation between the inflow velocity of the gas into the neutral point (V_{inflow}) and the rise velocity of the loop (V_{loop}) for different β models. (We also plot mean velocities in Table 3.) From this table, it seems that the inflow velocity is nearly comparable with the rise velocity regardless of β. Since the inflow velocity has not yet been observed, this relation may be used as a prediction or a guide for the inflow velocity.

5. DISCUSSION

Now we are ready to discuss how the main features of solar flares can be understood physically in the framework of the reconnection model on the basis of our results in § 3.

We discuss first the time evolution of the system during the impulsive phase. It is found that the plasmas surrounding the neutral point as well as between the slow shocks are strongly heated. Hence, thermal conduction should transport energy efficiently from this region to the lower atmospheres along the field lines, which works as heating of the lower atmosphere. Nonthermal electrons accelerated by unknown mechanisms can also heat the lower atmosphere. Atmospheric gas will then be evaporated into the upper atmosphere, filling the magnetic loops, thereby making the soft X-ray flaring loops, although the present simulations performed on the basis of the fluid approximation are unable to describe such phenomenon directly. The temperature near the neutral point is 8 times as large as the value outside the current sheet (see Fig. 10*a*). If the initial plasma β is sufficient low, $\beta \ll 0.1$, the temperature would be much higher because the converted thermal energy will increase. (Roughly, $T_{\mathrm{neutral\ point}} \propto B_0^2/8\pi$, so $T_{\mathrm{neutral\ point}}/T_{\mathrm{outside}} \propto (B_0^2/8\pi)/T_{\mathrm{outside}} \propto \beta^{-1}$.) Thus, it will be reasonable to think that such a very hot region can produce high-speed conduction flow.

Figure 10*a* shows that the loop-top region behind a fast shock has high density, about twice as dense as the ambient region. Temperature at the loop top is also enhanced by slow shocks and is about 6 times greater than that of the embedded region (Fig. 10*c*). The loop-top region is, hence, very likely to emit hard X-rays, which is consistent with the observations of the flares in the impulsive phase (see Masuda et al. 1994).

Next we discuss the gradual phase of the impulsive flares. Since thermal conduction and radiative cooling work well in this phase, the low-γ case is relevant in this phase. From Figures 11*a*–11*c*, we find a high-density region in the loop top, where the magnetic fields sink at the center (on the line of $x = 0$) and encompass the matter. We suggest that this dense region could be the source with long-lived thermal emission observed in the gradual phase (see Acton et al. 1992; Feldman et al. 1994).

As for the γ effect, the system with lower γ shows a more drastic evolution (see Fig. 12) (see also related works by Sato et al. 1992 and Yokoyama & Shibata 1993). So, if we assume that the intensity of high-energy radiation, such as hard X-rays, relates to the reconnection rate, which is somewhat rough assumption, it follows that thermal conduction should be efficient in flares exhibiting a rapid intensity variations. This implies that one of the characteristics of the impulsive flare may be an effective thermal conductivity.

Through discussions above, we may conclude that the reconnection model for the *cusp-type* flare can also explain many features of *non–cusp-type* flares observed in soft and hard X-rays. This reconnection model has been proposed and developed mainly for the *cusp-type* flares (see, for example, Forbes & Priest 1982; Forbes 1985; Forbes & Malherbe 1985, 1988). Figure 15 summarizes our view of the *cusp-type* flare in the impulsive phase (*left*) and in the gradual phase or LDE flares (*right*), respectively (see also the discussion on the "unified model" by Shibata et al. 1995).

In the impulsive phase, there are downward flows of high-energy electrons and thermal conduction originating from the neutral point and directing along the magnetic fields towards the chromosphere. These downflows form the conduction front (see Forbes & Malherbe 1985) and heat the neighboring plasmas. The chromospheric gas is heated and evaporates into the corona. Since the emissivity is more sensitive to density than temperature, very hot regions will not always be observed, unless density is very high. Thus, we conjecture that the soft X-ray bright loop could be a dense region filled with evaporated gas. The reconnection jet collides with the loop top, forming the hot and dense core which will emit hard X-rays. If the evaporated flow has not yet reached this energetic region, the hard X-ray source above the soft X-ray flaring loop will be observed.

In the gradual phase or LDE flare, thermal conduction would be efficient, and the reconnected loop under the neutral point would be sufficiently filled with the evaporated flow. The conduction front will heat up the material along the boundary of the loop, which leads to its observation as a bright cusp-type structure in soft X-rays. The loop-top source is observed to be embedded by these evaporated gases. As for the inside loops, heating is no longer effective so that the loops can cool via radiative cooling process, thereby forming Hα post-flare loops.

The system in the impulsive phase has a small diffusion region and shows the effective "Petschek-type" configuration, while in the gradual phase it has a long elongated

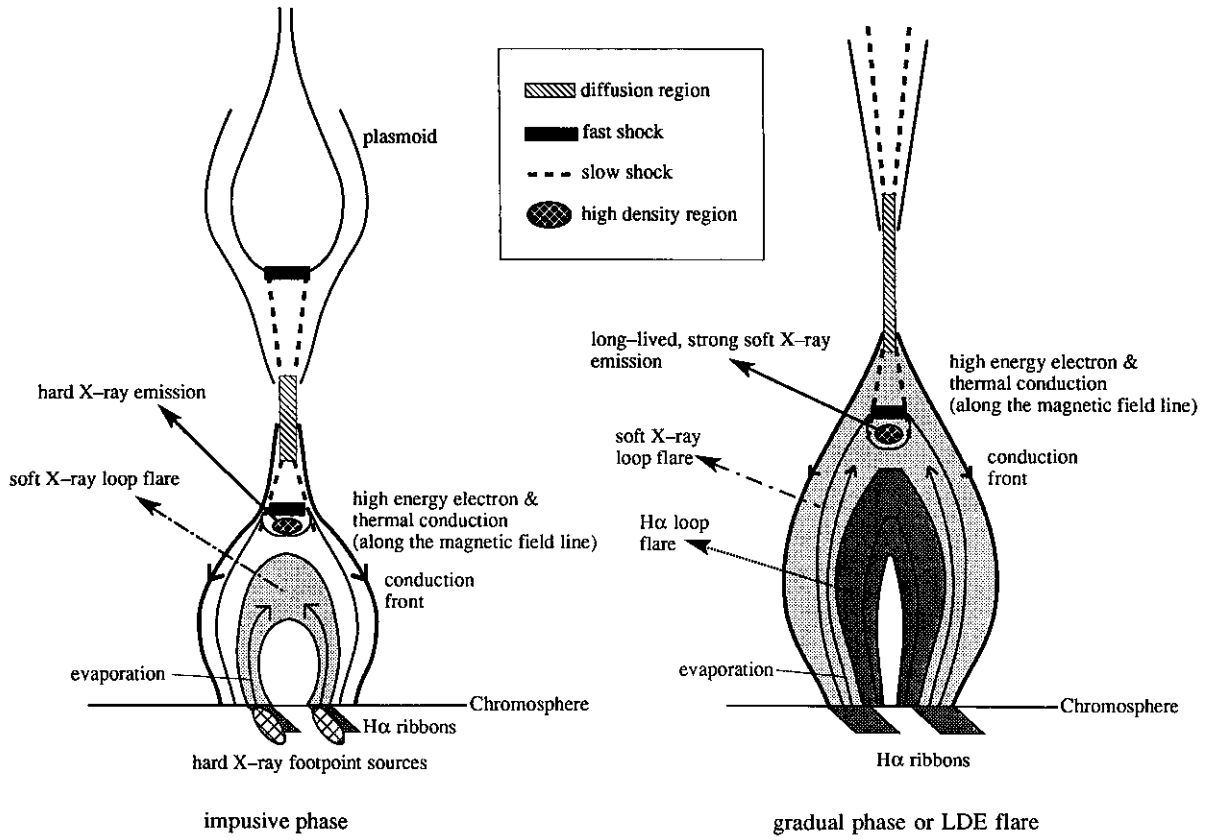

FIG. 15.—Schematic views of the cusp-type flare in the impulsive (*left*) and in the gradual phase of LDE flare (*right*), respectively. In the impulsive phase, a hard X-ray loop-top source is observed, whereas in the gradual phase or LDE flare thermal conduction and radiative cooling have effectively worked out so that there appears soft X-ray cusp structure associated with a long-lived soft X-ray loop-top source and Hα postflare loop. A conduction front is formed by the heat flow emerging from the vicinity of the neutral point directing toward the loop footpoint. From the lower atmosphere, the evaporated gases go upward and fill inside the loop.

diffusion region and shows the less effective "Petschek-type" configuration (see Petschek 1964). These configurations can explain the violent energy release in the impulsive phase and subsequent gradual relaxation in the gradual phase.

6. CONCLUSIONS

1. On the basis of the reconnection model, we have studied the structures of the *cusp-type* flares in detail. We found a high-temperature and density region at the loop top (below the neutral point), which is heated by slow shocks and confined by the magnetic pressure walls. These are in good agreement with the structures of the impulsive flares observed by *Yohkoh*.

2. A plasmoid with a high-density core is formed above the neutral point. It is surrounded by high-temperature boundary layers and moves upward. The motion of the plasmoid is quite sensitive to the initial density in the current sheet (ρ_c). The observed plasmoid velocity can be reproduced when we assign $\rho_c \simeq 40\rho_0$. Alternatively, perpendicular magnetic fields, if they ever exist, would prevent the upward motion of the plasmoid.

3. We have investigated the effect of plasma β on the evolution of the flare and found that the results are almost independent of β if velocity and timescale are normalized by V_{A0} and t_{A0}. This will help us to understand the nature of the flare in more realistic situations in which β is too small to study in the numerical simulation.

4. As reconnection proceeds, the height of the loop top moves upward with time as $z \propto t^{0.7}$. Hence, the loop rises rapidly at first and is then gradually decelerated later. This is consistent with the observations (see Pneuman 1981).

5. The relation between the inflow velocity and the rise velocity of loop was studied. They have almost the same values regardless of β.

6. When γ is near 1, which may simulate the case of efficient thermal conduction, the evolution of the system is more drastic than in the $\gamma = 5/3$ case. Moreover, plasma heating will be suppressed in general, but the compressional effect is more enhanced than in the $\gamma = 5/3$ case. In energetics, hence, magnetic energy is converted more efficiently into kinetic energy than thermal energy.

7. Our simulations can well account for the existence of the loop-top, hard X-ray sources discovered in the impulsive flares. We conclude that both the impulsive flares and the LDE flares can be understood in general by the reconnection model for the *cusp-type* flares.

More realistic calculations incorporating the effects of radiative cooling, thermal conduction, and perpendicular magnetic fields are necessary in future work, with which detailed comparisons with the observations will become possible. Moreover, the initial process of forming the current sheet should also be considered. This will help our understanding of the nature of solar flares in general.

We would like to thank the *Yohkoh* team members for supporting *Yohkoh* data. We also acknowledge the fruitful advice of S. Masuda, S. Tsuneta, and M. Ugai. The numerical computations have been carried out using FACOM VPX210/10S at the National Institute for Fusion Science.

REFERENCES

Acton, L. W., et al. 1992, PASJ, 44, L71
Alfvén, H., & Carlqvist, P. 1967, Sol. Phys., 1, 220
Carmichael, H. 1964, in AAS-NASA Symposium on Solar Flares, ed. W. N. Hess (NASA SP-50), 451
Feldman, U., et al. 1994, ApJ, 424, 444
Forbes, T. G. 1985, ApJ, 305, 553
Forbes, T. G., & Malherbe, J. M. 1985, ApJ, 302, L67
———. 1988, Sol. Phys., 120, 285
Forbes, T. G., & Priest, E. R. 1982, Sol. Phys., 84, 169
Hiei, E., & Hundhausen, A. J. 1996, in Magnetohydrodynamic Phenomena in the Solar Atmosphere, ed. Y. Uchida, T. Kosugi, & H. S. Hudson (Tokyo: Kluwer), in press
Hirayama, T. 1974, Sol. Phys., 34, 323
Kopp, R. A., & Pneuman, G. W. 1976, Sol. Phys., 50, 85
Masuda, S. 1994, Ph.D. thesis, Univ. Tokyo
Masuda, S., Kosugi, T., Hara, H., Tsuneta, S., & Ogawara, Y. 1994, Nature, 371, 495
Parker, E. N. 1979, Cosmical Magnetic Fields (Oxford: Oxford Univ. Press)
Petschek, H. E. 1964, in Proc. AAS-NASA Symp. on Solar Flares, NASA SP-50, 425
Pneuman, G. W. 1981, in Solar Flare Magnetohydrodynamics, ed. E. R. Priest (New York: Gordon & Breach), 379
Sato, T., & Hayashi, T. 1979, Phys. Fluids, 22, 1189
Sato, T., Hayashi, T., Watanabe, K., Horiuchi, R., Tanaka, M., Sawajiri, N., & Kusano, K. 1992, Phys. Fluids, B4, 450
Shibata, K. 1995, Adv. Space Res., 17, 415, 9
Shibata, K., Tajima, T., Steinolfson, R. S., & Matsumoto, R. 1989, ApJ, 345, 584
Shibata, K., et al. 1995, ApJ, 451, L83
Spicer, D. 1977, Sol. Phys., 53, 305
Sturrock, P. A. 1966, Nature, 211, 695
Tsuneta, S., Hara, H., Shimizu, T., Acton, L. W., Strong, K. T., Hudson, H. S., & Ogawara, Y. 1992, PASJ, 44, L63
Tsuneta, S., & Lemen, J. R. 1993, in Physics of Solar and Stellar Coronae, ed. J. Linsky & S. Serio (Dordrecht: Kluwer), 113
Uchida, Y., & Shibata, K. 1988, Sol. Phys., 116, 291
Ugai, M. 1986, Phys. Fluids, 29, 3659
———. 1995, Phvs. Fluids, submitted
Yokoyama, T., & Shibata, K. 1993, in Proc. Fourth Internat. Conference on Plasma Physics and Controlled Nuclear Fusion (ESA-SP 351), 203
———. 1994, ApJ, 436, L197

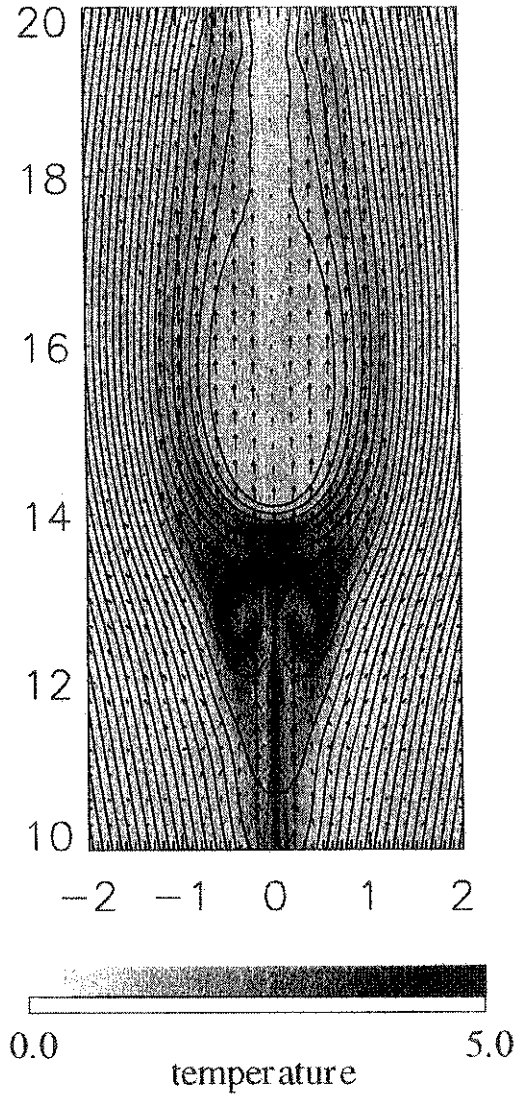

FIG. 6a

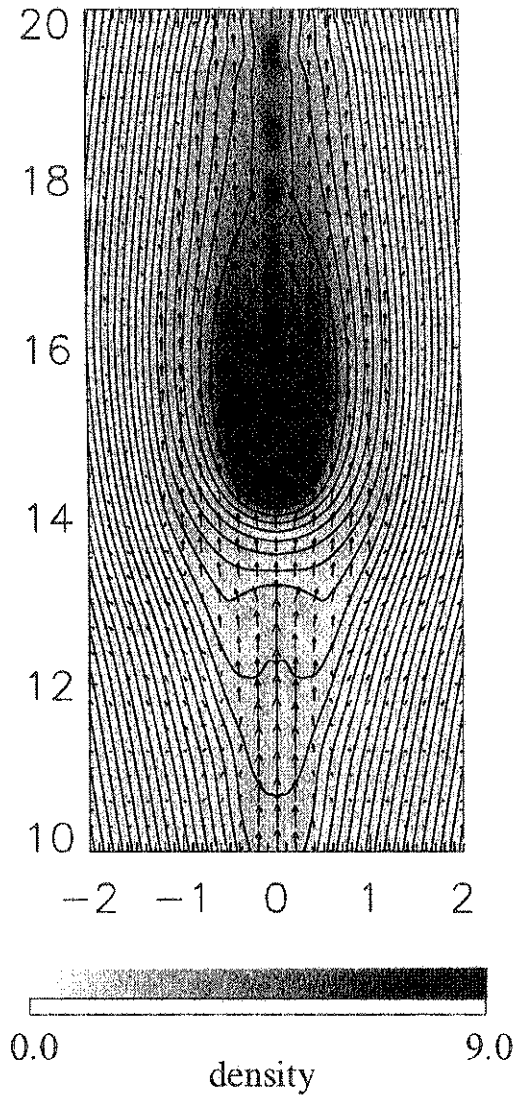

FIG. 6b

FIG. 6.—(*a*) Temperature contours of the plasmoid for the standard model (model S); solid lines and arrows represent magnetic field lines and velocity fields (normalized by V_{A0}), respectively. (*b*) Same as (*a*), but for density contours. Elapsed time $t = 16.0\,(L_0/C_{s0})$ in both panels.

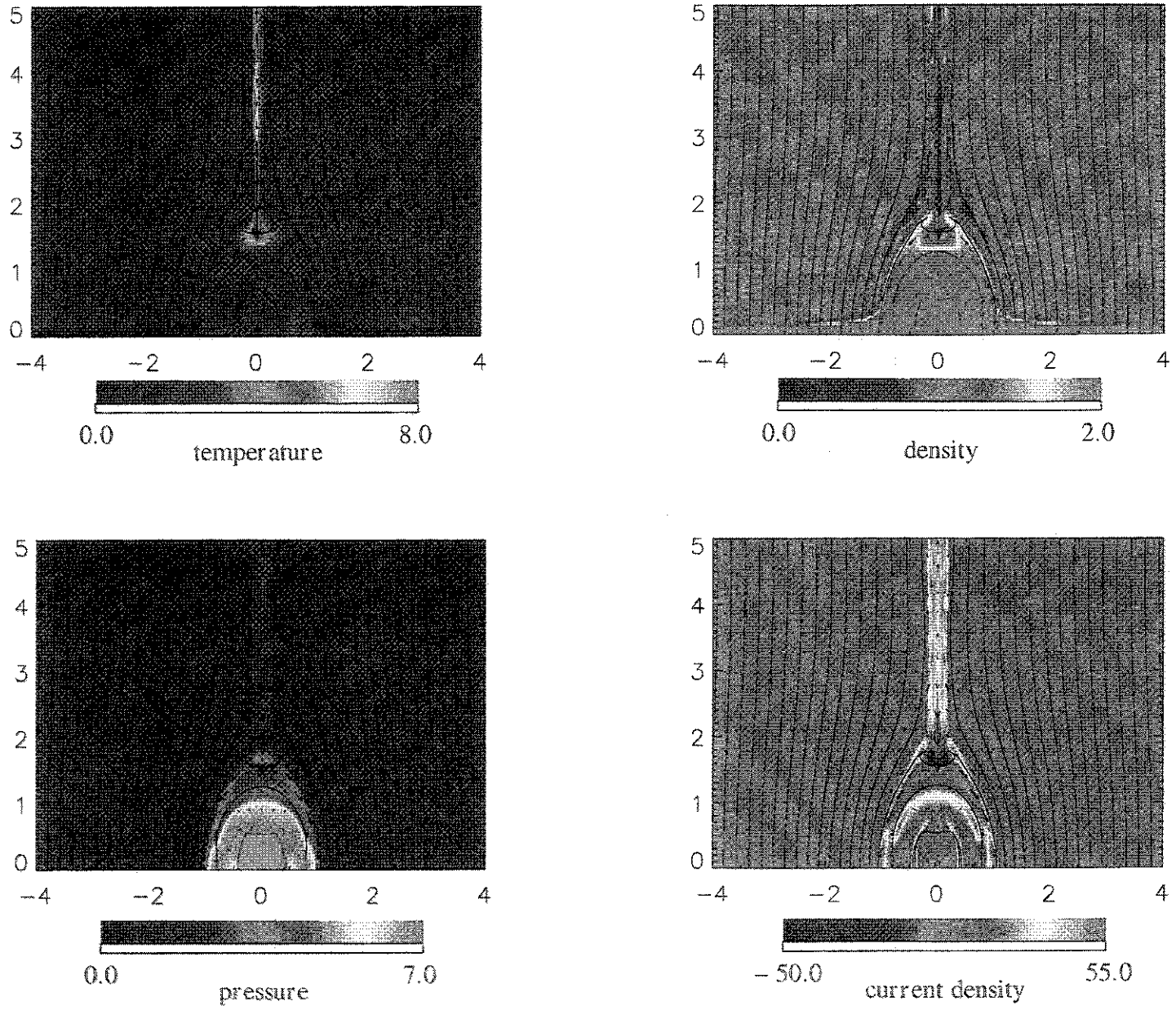

FIG. 10*a*

FIG. 10.—(*a*) Temperature (*top left*), density (*top right*), pressure (*bottom left*), and current density (*bottom right*) contours of the loop (model H1). Solid lines and arrows represent field lines and the velocity fields (normalized by V_{A0}), respectively. (*b*) Variations of temperature (T), density (ρ), gas pressure (Pg), the absolute value of the x-component of the magnetic field ($|Bx|$), and fast-mode Alfvén Mach number (Ma) along the z-axis. (*c*) Variations of temperature (T), density (ρ), current density (Jy), gas pressure (Pg), and magnetic pressure (Pm) along the horizontal line crossing the loop top. Time $t = 10.0$ in all cases.

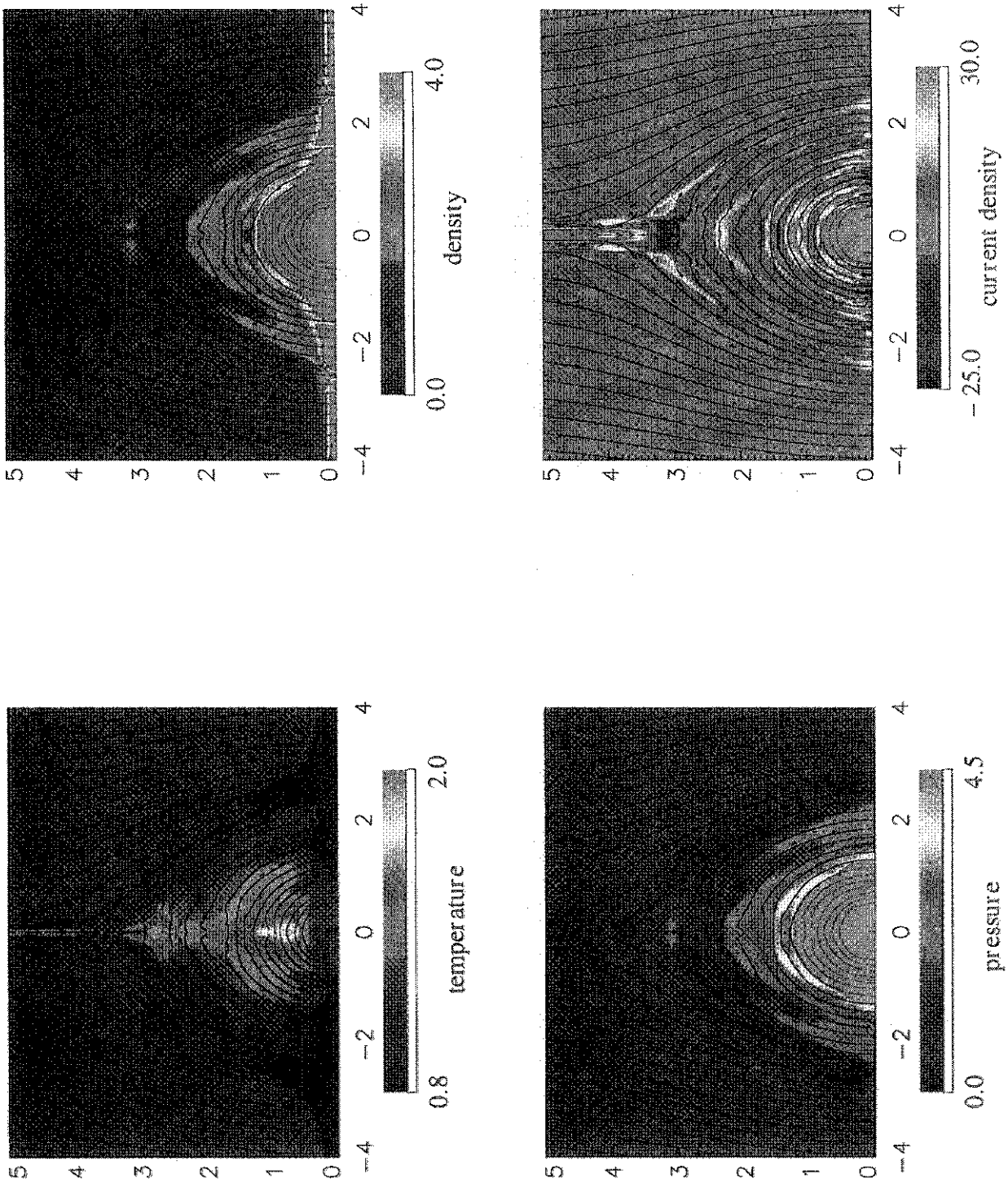

FIG. 11*a*

FIG. 11.—Same as Fig. 10, but for the low-γ model (model H2). Time $t = 19.0$ in all cases.